PCCP

Accepted Manuscript

ROYAL SOCIETY OF CHEMISTRY

www.rsc.org/pccp

The modified Quasi-Quantum Treatment of rotationally inelastic NO(X)-He scattering

Xia Zhang,[1] Chris J. Eyles,[2] Dajun Ding[1*] and Steven Stolte[1,3,4*]

[1]*Institute of Atomic and Molecular Physics, Jilin University, Changchun, 130012, China*
[2]*Institut fur Chemie und Biochemie, Freie Universitat Berlin, Takustrasse 3, 14195, Berlin, Germany*
[3]*Institute for Lasers, Life, and Biophotonics, Vrije Universiteit, de Boelelaan 1083, Amsterdam 1081 HV, The Netherlands.*
[4]*Laboratoire Francis Perrin, Bâtiment 522, DRECEM/SPAM/CEA Saclay, 91191 Gif sur Yvette, France*

*Corresponding Author: s.stolte@vu.nl; dajund@jlu.edu.cn

Abstract

A Modified Quasi-Quantum Treatment (MQQT) of molecular scattering has been developed to account for the softness of the repulsive part of the anisotropic atom-molecule PES. A contour of the PES is chosen such that the barrier height is just large enough to reflect the incoming kinetic energy, directed anti-parallel to the hard shell normal at the site of impact. The resulting rotationally inelastic quantum state resolved DCSs and ICSs of He + NO(X) at $E_{col} = 508\ cm^{-1}$ are compared to those obtained from regular QQT and from Quantum Mechanically exact calculations performed on the full highest quality ab initio Vsum PES. The MQQT parity changing DCSs for $\Delta j \leq 4$ exhibit much better agreement with the QM DCSs than is obtained using regular QQT, particularly in the forward scattered direction. The improvements upon the remaining MQQT DCSs with respect to the regular QQT was minor, due to the near incompressible hard shell character of the $n \neq 1$ or 3 anisotropic Legendre polynomial terms of the PES.

1. Introduction

The Regular Quasi-Quantum Treatment (RQQT) of the rotationally inelastic collision problem, introduced by Gijsbertsen *et al.*,[1] succeeded for the first time to clarify the physical mechanism behind the remarkable sign alternation of the steric asymmetry (SA) of the rotationally inelastic Integral Cross Section (ICS) between even and odd changes in the rotational quantum number *j*. Such changes were observed and theoretically predicted for the NO(X)-Ar,[2, 3] and NO(X)-He[4] collision systems. Moreover RQQT also revealed that the angular dependence of the Differential Cross Sections (DCSs) to neighboring rotational states of NO(X) with the same parity are nearly identical.[1, 5-8] Assuming an anisotropic convex hard shell potential that mimics the repulsive core of the *ab initio* NO(X)-RG V_{sum} PES,[9, 10] RQQT ought also to be able to predict both the spin orbit conserving and changing quantum state resolved rotationally inelastic DCSs.

Applying the RQQT, Taatjes *et al.*[11] were able to take measurements of the SA and Λ-doublet propensities provided by experimentally observed rotationally inelastic NO(X)-D_2 ICSs, and to extract from these a realistic hard shell PES, which provided a good match to the NO(X) – D_2 experimental values.

Ballast *et al.*[7] provided a more systematic basis for the hitherto intuitive formulation of the RQQT of the rotationally inelastic collision problem, and extended RQQT to collisions of an atom with a closed shell linear molecule. The resulting RQQT DCSs for Ne-CO ($X^1\Sigma$) and for He-NO ($X^2\Pi$) compared well with the exact QM DCSs calculated at a collision energy of respectively 511 cm^{-1} (63.4 meV)[12] and 514 cm^{-1} (63.7 meV).[13]

The RQQT has also been the subject of recent development, with Zhang *et al.*[14] obtaining a general scaling rule for the collision energy dependence of a rotationally inelastic DCS, and also extending the calculation of the RQQT DCSs from the classically allowed region into the classically forbidden range of small scattering angles. The rotationally inelastic quantum state resolved NO-He DCSs at a collision energy E_{col}= 508 cm^{-1}(63meV) of the present paper served as the focus of their study.

The Modified Quasi-Quantum Treatment (MQQT) of the present study, in common with RQQT, is numerically extremely efficient[15]. RQQT has already been successfully employed to provide insight into the distinct interference structures reflecting different sensitivities to specific terms in the interaction potential.[5, 6, 16-18]

The velocity-mapped[19] ion imaging method,[20] pioneered on the HCl-Ar system at a collision energy of E_{col} = 66.7meV (538 cm^{-1})[21] and later extended to Ne, Kr, N_2 and CH_4 as collision partners,[22] provides a convenient means by which the quantum state resolved rotationally inelastic DCSs can be measured.

This method of observing quantum state resolved rotationally inelastic DCSs has been extended to an appreciable number of collision systems, and the resulting experimentally determined DCSs have subsequently been compared with numerically exact QM DCSs obtained on state of the art *ab initio* calculated PESs.

The remainder of this paper is organized as follows. The MQQT of the rotationally inelastic collision problem is described in Section 2. The Legendre expansion coefficients of the MQQT V_{sum} PES[10], the phase shift curves, scattering amplitudes and finally the quantum state resolved rotationally inelastic differential and integral cross sections calculated for the NO(X)-He collision system at $E_{col} = 508\ cm^{-1}$ (63.0 meV) are presented and discussed in Section 3. The main conclusions and outlook for the future are then given in Section 4.

2. Method

The regular QQT theory has been described in previous studies, and only the essentials necessary to inform the reader of the methodology[1, 7, 14] and relevance of MQQT are given below. Appendix A of the electronic supporting information (ESI) provides specific methodological details and additional information.

The numerically exact QM solution of the Schrödinger equation for the rotationally inelastic collision problem utilizes the full range of the PES, and expands the incoming plane wave into spherical waves. This transforms the collision problem into a large set of coupled differential equations covering all relevant $j,l,\bar{\Omega},\varepsilon,j',l',\bar{\Omega}',\varepsilon'$ scattering channels, which are numerically solved at each permitted value of the total angular momentum quantum number *J*, to obtain a series of $S^{J}_{j,l,\bar{\Omega},\varepsilon;j',l',\bar{\Omega}',\varepsilon'}$ matrix elements, in which *j* is the rotational angular momentum quantum number, *l* is the orbital angular momentum quantum number, $\bar{\Omega}$ is the absolute value of the projection of the electronic angular momentum onto the molecular axis

and ε is the symmetry index which labels the lower(upper) Λ-doublet level with ε=1 (ε= -1). The $\varepsilon = \pm 1$ rotational sublevels differ in parity by a factor of $P = \varepsilon(-1)^{j-\frac{1}{2}}$. Primed quantum numbers denote the final state. Often one has to couple about one thousand channels up to a thousand times to obtain the scattering amplitude $f_{j=0.5,m,\bar{\Omega}=0.5,\varepsilon\to j',m',\bar{\Omega}',\varepsilon'}(\theta)$. Such multiple coupled differential equations and summations between channels are avoided in RQQT and MQQT. Both of these method bypass the calculation of the S-matrix elements and approximate the scattering amplitude $f_{j=0.5,m,\bar{\Omega}=0.5,\varepsilon\to j',m',\bar{\Omega}',\varepsilon'}(\theta)$ directly. The rotationally inelastic transition probability amplitude is obtained by sandwiching a phase shift function between the "bra" of the final and the "ket" of the initial rotational quantum state wavefunction. The so-called kinematic apse frame is employed, in which the momentum transfer vector,

$$\boldsymbol{a} \equiv \boldsymbol{k}' - \boldsymbol{k} \tag{1}$$

serves as the quantization axis along which the projection quantum numbers of j and of j' are m_a and m_a'. The direction of $\hat{\boldsymbol{a}}$, residing in the $\boldsymbol{k}$ and $\boldsymbol{k}'$ azimuth scattering plane, with respect $\boldsymbol{k}$ is denoted by the spherical angles β and $\alpha = \phi$. The spherical angles (γ_a, ϕ_a) of the molecular axis $\boldsymbol{r}$ with respect to $\hat{\boldsymbol{a}}$ provide the primary variables defining the geometry of the instantaneous impact onto the hard shell PES surface at $R_S(\gamma_a, \phi_a)$, effecting the transfer of the incoming state $|j = 0.5, m_a, \bar{\Omega} = 0.5, \varepsilon>$ to the outgoing state $<j', m_a', \bar{\Omega}', \varepsilon'|$. The normal $\hat{\boldsymbol{n}}$ to the shell surface at the point $R_S(\gamma_a, \phi_a)$ and $\hat{\boldsymbol{a}}$ are identical.[1,7] The component of the incoming wave vector $\boldsymbol{k}$ parallel to the shell surface at $R_S(\gamma_a, \phi_a)$ remains conserved,[23] *i.e.* $k_{\parallel} = k_{\parallel}'$. Conversely, the component $k_{\perp}$ of $\boldsymbol{k}$ directed anti parallel to $\hat{\boldsymbol{a}}$ is not generally conserved throughout the collision, and the maximum amount of the available collision energy E_{col} that can be transferred into rotation is limited to $E_{col} \cdot (\cos\beta)^2$. The projection quantum number m_a of j onto $\hat{\boldsymbol{a}}$ remains conserved throughout the collision event.[1, 14, 24, 25] The former restriction limits the range of β for which the transition from the rotational ground state $j = \frac{1}{2}$ with $E(j = \frac{1}{2}) \equiv 0$ to the rotationally excited j' state with $E(j')$ is allowed to

$\beta_\kappa \le \beta \le 180°$ [14], where

$$\beta_\kappa = \arccos(-\sqrt{1-(k'/k)^2}) = \arccos(-\sqrt{E(j')/E_{col}}) \quad (2)$$

The function $\cos\beta(\cos\theta)$ reaches its maximum at $\theta = \theta_\kappa$:[14]

$$\theta_\kappa = \arccos(k'/k) \quad (3)$$

We define an index *p*, such that *p*=2 if $0 \le \theta < \arccos(k'/k)$, corresponding to a classically forbidden (but Feynman path allowed) transition for which $\boldsymbol{k}'_\perp \uparrow\uparrow \boldsymbol{k}_\perp$ and *p*=1 if $\arccos(k'/k) \le \theta \le 180°$,[14] corresponding to a classically allowed transition for which $\boldsymbol{k}'_\perp \downarrow\uparrow \boldsymbol{k}_\perp$. The relation between $k'_\perp$ and $k_\perp$ depends on the rotational eigen-energy of the scattered NO molecule $E(j')$, defined relative to $E(j) \equiv 0$, and is given by:[14]

$$k'_\perp = \sqrt{(k_\perp)^2 - \tfrac{2\mu}{\hbar^2}E(j')} \quad (4)$$

The MQQT PES contour $R_S^{\mathrm{mod}}(\cos\gamma_R;\cos\beta)$ is chosen such that the height of the potential energy barrier is just sufficient so as not to be surpassed by the effective collision energy $E_{col}\cdot\cos^2\beta$,

$$V[R_S^{\mathrm{mod}}(\cos\gamma_a;\cos\beta)] = E_{col}\cdot\cos^2\beta \quad (5)$$

The MQQT hard shell contours $R_S^{\mathrm{mod}}(\cos\gamma_a;\cos\beta)$ at β =100º and β =170º obtained from the *ab initio* NO(X)-He $V_{sum}(R,\gamma_R)$ PES calculated by Kłos et al are shown in Fig.1.[10] The varying shell shape and size probed by (classically allowed, *p*=1) quite forwards β =100º and by quite backwards β =170º scattered near elastic collision events are visualized in back and red respectively. Overall, the radius of the $R_S^{\mathrm{mod}}[\cos\gamma_R;\cos(\beta=100°)]$ shell is about 0.8 Bohr larger than that of the $R_S^{\mathrm{mod}}[\cos\gamma_R;\cos(\beta=170°)]$ shell. This difference is almost as large as the De Broglie wavelength (1.16 Bohr) of the incoming wave vector $\boldsymbol{k}$ at E_{col} = 508 cm^{-1}.

Less pictorial but more detailed information is provided in Fig.2. It displays both the dependence of $R_S^{\mathrm{mod}}(\cos\gamma_R;\cos\beta)$ on $\cos\gamma_R$ and $R_S^{\mathrm{mod}}(\cos\gamma_a;\cos\beta)$ on $\cos\gamma_a$ for a number of individual β values covering the range from β =90º to β =180º. At $\gamma_a \approx \arccos(-0.086) = 95°$ the $R_S^{\mathrm{mod}}[\cos\gamma_a;\cos(\beta=90°)]$ contour is no longer uniquely defined by a single convex shape. The smooth He-NO (X) PES contours $R_S^{\mathrm{mod}}(\cos\gamma_a;\cos\beta)$ are found to be partially concave for $90° \le \beta < \beta_{\min}^{convex} = 101.45°$ and purely convex for $\beta \ge \beta_{\min}^{convex} = 101.45°$. Note that at each β there are three values of $\cos\gamma_R$ at which $R_S^{\mathrm{mod}}(\cos\gamma_a;\cos\beta) = R_S^{\mathrm{mod}}(\cos\gamma_R;\cos\beta)$ both at $\cos\gamma_R = \pm 1$

and at $0.1 \le \cos\gamma_R \le -0.05$. It is within the latter range of $\cos\gamma_R$ that the dependence of $R_S^{\mathrm{mod}}(\cos\gamma_a;\cos\beta)$ upon $\cos\gamma_a$ is the most distinct from that upon $\cos\gamma_R$. Specifics details concerning the MQQT phase shift, scattering amplitude, DCS and ICSs, defined consistently to those of RQQT (but distinct from QM) are given in Section IA of the ESI.

3. Results and Discussions

3.1 Phase shift curves and scattering amplitudes

To gain insight into the distinctive features of the rotationally inelastic MQQT DCSs compared to those of the RQQT (and also into their underlying Legendre anisotropy coefficients $C_n(\cos\beta)$ of the PES, specified and discussed in Section IB of the ESI), the $\cos\gamma_a$ dependency of the phase shifts $\eta^{\mathrm{mod}}_{E=0\to E(j'=4.5)}(\gamma_a;\beta.p)$ and $\eta^{reg}_{E=0\to E(j'=4.5)}(\gamma_a;\beta,p)$ have been explored over their kinematic range:[14]

$$-1 \le \cos\beta \le \cos\beta_\kappa \tag{6}$$

Note that in the case of RQQT, $R_S^{reg}(\cos\gamma_a) \equiv R_S^{\mathrm{mod}}(\cos\gamma_a;\beta=180°)$ does not depend on β. In Fig. 3 the $\cos\gamma_a$ dependence of the MQQT and RQQT phase shift curves of the $j=\frac{1}{2}\to j'=\frac{7}{2}$ inelastic transition is shown for a number of representative apse angles β (chosen to coincide with the $\beta \ge 103°$ angles depicted in Fig. 2), for both classically allowed (p=1) and classically forbidden (p=2) pathways. These representative apse angles facilitate a comparison of the p=1 and p=2 phase shift curves in relation to the specifics of the probed PES contour. Eq (I.4) (Section IA of the ESI) shows that the p=2 phase shift is a factor if $\{|\cos\beta| - \sqrt{\cos^2\beta - E_{j'}/E_{col}}\}/\{|\cos\beta| + \sqrt{\cos^2\beta - E_{j'}/E_{col}}\}$ smaller than the p=1 phase shift. The MQQT and RQQT phase shifts shown in Figs. 3 and 4, (as obtained from Eq.(I.1)), are shown as solid and dashed curves, respectively. To facilitate comparison of the modified $\eta^{\mathrm{mod}}_{j=0.5\to j'=7.5}(\gamma_a;\beta,p)$ and regular $\eta^{reg}_{j=0.5\to j'=7.5}(\gamma_a;\beta,p)$ phase shifts on β and p, the maximal values in Figs. 3 and 4 have been shifted to unity. This was done by the addition or subtraction of the proper γ_a independent phase shift. Eqs.(I.8-I.15) (Section IA of the ESI) show that both the apse and collision frame RQQT and MQQT inelastic DCSs are independent of such a constant shift.

As in the full QM approach, in QQT the classical lever due to the γ_a - dependent impact

of the He atom onto the He-NO(X) PES contour has no direct relevance on the outcome of the scattering event. Both the QM scattering amplitude and the MQQT scattering amplitude of Eq.(I.8) (Section IA of the ESI), depend on the interference between all Feynman allowed paths from the initial rotational quantum state to the final rotationally excited quantum state at a particular classically allowed (p=1) or classically forbidden (p=2) apse angle β, or at the equivalent scattering angle θ.[1, 7, 14] One of the most striking features in Fig. 3 is the similarity of the $\eta^{\mathrm{mod}}_{j=0.5\rightarrow j'=2.5}(\gamma_a;\beta,p)$ and $\eta^{reg}_{j=0.5\rightarrow j'=2.5}(\gamma_a;\beta,p)$ phase shifts for negative $\cos\gamma_a$ O-end impact sites of the He-atom onto the hard shell contour PES, while the phase shifts differ more strongly at positive $\cos\gamma_a$ N-end impact sites.

To allow a clear differentiation between the N-end part and the O-end part of a particular He-NO β-dependent PES contour, the $\cos\gamma_a=\cos\gamma_a^{waist}$ edge was chosen to coincide with the "waist" of the $R_S^{\mathrm{mod}}(\cos\gamma_a;\beta)$ shell contour. The value of $\cos\gamma_a^{waist}$ follows from:

$$\frac{\partial R_S^{\mathrm{mod}}[\cos\gamma_a=\cos\gamma_a^{waist};\beta]}{\partial\cos\gamma_a}=0 \quad ; \quad \cos\gamma_a^{waist}\neq\pm1 \tag{7}$$

The details of the MQQT and RQQT p=1 phase shift curves around the $\cos\gamma_a=\cos\gamma_a^{waist}$ impact region are shown in Fig. 4. The MQQT and the RQQT phase shifts are both proportional to a $K(\beta,p)$ kinetic factor, given by Eq.(I.2) (Section IA of the ESI). The left panel of Fig.4 shows that when β increases from 100° to 180° the MQQT value of $\cos\gamma_a^{waist}$ shifts from -0.085 to -0.054. Since $R_S^{reg}(\cos\gamma_a)\equiv R_S^{\mathrm{mod}}(\cos\gamma_a;\beta=180°)$ all RQQT phase shift curves in the right panel of Fig. 4 maximize at $\cos\gamma_a^{waist}=-0.054$.

Dynamically the near similarity of the O-end MQQT and RQQT phase shifts reflects the more closed shell character of the NO(X) molecule at this impact region. As discussed in more detail in Section IB of the ESI, the π* orbital of the NO molecule possesses a smaller and less extended one electron charge density at the O-end than at the N-end region.[10] This phenomenon is also responsible for the anomalous direction of the $^{-}NO^{+}(X)$ electric dipole moment. The same phenomenon causes the difference between the RQQT and MQQT phase shifts for all scattering angles with β <180º to maximizes at $\cos\gamma_a\cong0.5$, as shown in Fig. 3. The orbital symmetry node in the π* lobe along the NO axis causes the differences between the MQQT and RQQT phase shifts to become minimal at $\cos\gamma_a=\pm1$, where the π* orbital

electron density drops to zero. When β approaches 180º the MQQT and RQQT phase shifts become similar. By definition in both panels the $\beta = \beta_\kappa = 103°$ phase shift curves are identical.

The MQQT apse frame scattering amplitude $g^{\mathrm{mod}}_{j=0.5,m_a,\bar{\Omega}=0.5,\varepsilon\to j',m'_a,\bar{\Omega}'=0.5,\varepsilon'}(\beta,p)$ also depends on the geometric scattering amplitude, $g^{\mathrm{mod}}_{geom}[\gamma_a;\beta]$, which constitutes an additional γ_a-dependent factor in the integrand of Eq.(I.5) (see Section IA of the ESI). Ballast et al, previously explored the so-called constant curvature approximation in which a γ_a independent geometrical scattering amplitude[7]

$$g^{reg}_{concur}(\cos\beta) \equiv \sqrt{|\cos\beta|[R^{\mathrm{mod}}_0(\cos\beta=-1)]^2} \tag{8}$$

was used instead of $g^{\mathrm{mod}}_{geom}(\gamma_a;\beta)$ in the integrand of Eq.(I.5) (Section IA of the ESI), where $R^{\mathrm{mod}}_0(\cos\beta=-1)$ denotes the averaged value of $R^{\mathrm{mod}}_S(\gamma_a;\cos\beta=-1)$. The constant curvature approximation leads to slightly smaller DCSs for low values of Δj than when the full γ_a-dependent $g^{\mathrm{mod}}_{geom}[\gamma_a;\beta]$ is used. The small differences between the resulting absolute values of the DCSs were found to disappear at $\Delta j > 8$.[7] For this reason, the γ_a-dependency of $g^{\mathrm{mod}}_{geom}[\gamma_a;\beta]$ is expected to be of minor influence on the outcome of $g^{\mathrm{mod}}_{j=0.5,m_a,\bar{\Omega}=0.5,\varepsilon\to j',m'_a,\bar{\Omega}'=0.5,\varepsilon'}(\beta,p)$, validating the approximation of $g^{\mathrm{mod}}_{geom}(\gamma_a;\beta)$ with $g^{\mathrm{mod}}_{concur}(\cos\beta)$, where

$$g^{\mathrm{mod}}_{concur}(\cos\beta) \equiv \sqrt{|\cos\beta|[R^{\mathrm{mod}}_0(\cos\beta)]^2} \tag{9}$$

It is the phase shift function $\exp[i\eta^{\mathrm{mod}}_{j=0.5\to j'}(\gamma_a;\beta,p)$ which most strongly determines the β and p dependency of $g^{\mathrm{mod}}_{j=0.5,m_a,\bar{\Omega}=0.5,\varepsilon\to j',m'_a,\bar{\Omega}'=0.5,\varepsilon'}(\beta,p)$, and hence the angular dependence of the DCS. Eqs (I.6-I.8) (Section IA of the ESI) and Eq. (9) incorporate the constant curvature approximation into the expression for the MQQT scattering amplitude yielding:

$$g^{\mathrm{mod}-concur}_{j=0.5,m_a,\bar{\Omega}=0.5,\varepsilon\to j',m'_a,\bar{\Omega}'=0.5,\varepsilon'}(\beta,p)\cdot C(\beta) =$$

$$= \delta_{m_a,m'_a}\sqrt{j'+\tfrac{1}{2}}\cdot\tfrac{m_a}{|m_a|}\, g^{\mathrm{mod}}_{concur}(\cos\beta)\cdot\tfrac{1}{2}\int_{-1}^{1} d\cos\gamma_a \cdot \exp[i\eta^{\mathrm{mod}}_{j=0.5\to j'}(\gamma_a;\beta,p)]\cdot P_{j'-\varepsilon'\varepsilon/2}(\cos\gamma_a) \tag{10}$$

The relation between the MQQT (and RQQT) apse frame scattering amplitude and the collision frame differential cross section, $\frac{d\sigma^{\mathrm{mod}}_{j=\frac{1}{2},\varepsilon\to j',\varepsilon'}}{d\omega}(\theta)$, are given in Eqs.(I.7) and (I.11) (Section 1A of the ESI). Upon integration over the full range of scattering angles one obtains the related integral collision cross sections $\sigma^{\mathrm{mod}}_{j=\frac{1}{2},\varepsilon\to j',\varepsilon'}$.

3.2 Differential and integral rotationally inelastic cross sections

The MQQT, RQQT and exact QM rotationally inelastic spin-orbit manifold conserving NO(X, v=0)-He inelastic DCSs, for the transitions $j=\frac{1}{2},\varepsilon=-1\to j'=\frac{1}{2},\varepsilon'=1$ and $j=\frac{1}{2},\varepsilon=-1\to 1.5\le j'\le 11.5,\varepsilon'=-1$ at E_{col} =508cm^{-1}, are shown in Fig. 5. The exact QM DCSs obtained from the HIBRIDON code were provided by Kłos *et al.*[17] The rapid oscillatory structures present in the QM DCSs at small scattering angles for $\Delta j<5$ arise from diffraction effects, which are not accounted for in either RQQT or MQQT. In place of the QM diffraction pattern, the QQT DCSs exhibit a sharp peak at $\theta=0$, due to a dramatic difference in weighting factors between β and θ, which for $\Delta j<5$ supersedes the maximum in the classically allowed (p=1) $\theta>\theta_{\kappa}$ range by orders of magnitudes. This difference decreases with increasing Δj, as the peak in the DCS at $\theta=0$ becomes relatively less significant.[14] The QM DCS calculation utilizes the full PES, while the RQQT simplifies the PES to a rigid hard shell given by $V_{sum}(R,\cos\gamma_R)=E_{col}$. The MQQT instead reduces the full PES with a hard shell PES contour, which is set equal to the amount of collision energy provided by the component of the incoming momentum vector directed anti-parallel to the surface normal, such that

$$V_{sum}(R,\cos\gamma_R,\cos\beta)=E_{col}\times\cos^2\beta \qquad (11)$$

Figure 5 shows that all RQQT NO(X)–He DCSs with $\Delta j\le 6$ are typically smaller than the exact QM DCSs in the classically allowed (p=1) forward scattered region. It is this difference, which becomes most substantial for the parity changing $\Delta j\le 4$ inelastic transitions, that stimulated the development of the MQQT DCS model, for which PES

contours range from $V_{sum}(R,\cos\gamma_a)=0$ for a glancing ($\cos\beta$=0) collision down to $V_{sum}(R,\cos\gamma_a)=E_{col}$ for a head on ($\cos\beta$=-1) collision. The effective larger size of the ellipsoidal potential at small scattering angles acts to increase the DCS in this region, reducing the discrepancy between the MQQT and QM results.

Figure 5 also shows that the p=1 range of the MQQT DCSs (particularly for the parity changing rotationally inelastic transitions for $\Delta j \le 5$) provide a much better approximation to the QM data than that provided by the RQQT. MQQT preserves the generally good agreement between RQQT and QM for transitions with $\Delta j > 5$.

Since it is the magnitude of the $C_{n=1}(\cos\beta)$ first order Legendre polynomial expansion coefficient (depicted in Fig.A, Section IB of the ESI), which varies the most at the low perpendicular collision energies for which $|\cos\beta| << 1$, the enhancement of the MQQT DCSs with respect to the RQQT DCSs continues up to scattering angles as large as 120º. This effect is by far the largest for the classically allowed p=1 parity paired $j=\frac{1}{2},\varepsilon=-1\rightarrow j'=\frac{1}{2},\varepsilon'=1$ and $j=\frac{1}{2},\varepsilon=-1\rightarrow j'=\frac{3}{2},\varepsilon'=-1$ DCSs in Fig.5.

In Section I.B of the ESI it is argued that the angular dependence of the MQQT and RQQT inelastic DCSs are independent of $C_{n=0}(\beta)$. All other $C_n(\cos\beta)$ coefficients shown in Fig. A (Section IB of the ESI) remain essentially stationary when $E_{col}\cdot\cos^2\beta \ge 326\ cm^{-1}$ or when $\Delta j \ge 13$. The near stationary nature of these coefficients for apse frame angles $\beta \ge$143º underlies the similarity between the MQQT and RQQT DCSs at scattering angles θ that correspond to $\beta \ge$143º. More specifically, this similarity ought to persist for the full range of θ wherever $\beta_\kappa > 143°$ *e.g.*, for $\Delta j > 12$.

To facilitate the visual comparison of the MQQT and RQQT DCSs with the QM data, the latter are multiplied by a numerical factor chosen such that all QM ICSs are scaled to the RQQT values. The MQQT and RQQT DCSs shown in Fig. 5 are very close to one another for parity conserving $\Delta j \ge 8$ transitions, implying that the n=1, and n=4 $C_n(\beta)$ coefficients (shown in Fig. A, Section IB of the ESI) are of minor importance only in determining these DCSs.

The rotationally inelastic DCSs of the classically forbidden p=2 range of scattering angles

i.e. from $\theta = 0°$ to $\theta = \theta_\kappa$ (within which β decreases from $\beta = 180°$ to $\beta = \beta_\kappa$), follows from similar expressions to those defining the classically allowed p=1 region of the DCSs for which θ ranges from $\theta = 180°$ to $\theta = \theta_\kappa$. In contrast to the p=1 range, the p=2 range of the MQQT and RQQT DCSs exhibit the best agreement when $\theta << \theta_\kappa$ and become most dissimilar if $\theta \to \theta_\kappa$. The absolute value of the p=2 phase shift of the QQT scattering amplitude is smaller than the corresponding p=1 phase shift, as specified by Eq.(I.4) (Section IA of the ESI). Additionally Eq.(I.15) (Section IA of the ESI) causes the classically forbidden part of the low Δj QQT DCSs to peak sharply at θ=0 and thereafter to drop strongly with θ. This classically forbidden region provides an analogue to the diffractive contribution to the QM DCSs in the forward scattered direction. For transitions with $\Delta j \geq 5$, Eq.(I.16) (Section IB of the ESI) brings about a slower drop-off of the QQT DCSs in the classically forbidden region $\theta < \theta_\kappa$ which has no obvious QM equivalent, and is best regarded as an artifact. However, the inclusion of the classically forbidden part of the DCSs results in only a minor change in the flux normalization coefficients C_{flux}^{mod} in Eq.(I.11) and Eq.(I.12) (Section IB of the ESI). Similarly, the classically forbidden forward scattered artifact peak in the QQT DCS leads only to a marginal contribution to the total inelastic cross section.

Although the V_{sum} PES of the NO(X)-He rotationally inelastic collision system consists of a shallow well followed by a compressible repulsive wall, the difference between the RQQT and MQQT DCSs is mostly limited to near forward scattering angles and was found to become marginal for Δj>6. All anisotropic $C_{n>0}(\cos\beta)$ Legendre coefficients shown in Fig. A (Section I.B of the ESI) become nearly stationary when $E_{col}\cos^2\beta > E(j'=7.5)$ or for $\beta > 117.04°$. For transitions with $j' \geq 7.5$ one has $\cos\beta_\kappa < \cos(117.04°)$, which implies that the MQQT DCSs become essentially identical to the RQQT DCSs. This is because the anisotropic terms of the NO(X)-He PES do not vary significantly over the range $E(j'=7.5) = 105.36\ cm^{-1} \leq V_{sum}(R,\gamma_R) \leq 508\ cm^{-1}$.

Figure 6 compares the j' dependence of all $j = \frac{1}{2}$ $\varepsilon' = \varepsilon = -1$ $E_{col} = 508\ cm^{-1}$ MQQT NO(X) – He ICSs with those obtained from RQQT and exact QM calculations. At low values of Δj, all ICSs show pronounced oscillatory structures, which disappear with increasing j'.

At low Δj, especially for parity changing $(-1)^{j'-\varepsilon\varepsilon'/2} < 0$ transitions, the rotationally inelastic MQQT ICSs are larger than the RQQT ones, which reflects the less pronounced maximum in the RQQT DCSs. The agreement between the MQQT and exact QM ICSs is less convincing, as expected[51], than that obtained for the scattering angle dependence of the DCSs. The MQQT hard shell PES approximation accounts only for the hard shell repulsive $C_{n=2}(\cos\beta)$ expansion coefficient and lacks the contribution (present in the full QM treatment) of the anisotropic attractive long range $V_2(R)\cdot P_2(\cos\gamma_R)$ term of the V_{sum} PES.[10] This contribution causes the QM ICS for the transition $j = 0.5,\ \varepsilon = -1 \rightarrow j' = 2.5,\ \varepsilon = -1$ to become around twice as large as the MQQT and RQQT ICSs. In Fig.4 where the QM DCS was scaled to the RQQT ICS, this contribution is reflected in the enhanced forward scattering of the QM DCS with respect to the MQQT and RQQT DCSs.

4. Conclusions and Outlook

The MQQT of the rotationally inelastic collision problem developed in the present study employs a modified hard shell potential contour, defined as $V_{sum}(R,\gamma_R) = E_{col}\cdot\cos^2\beta$, which depends on the polar angle β between the surface normal ***a*** and the incoming momentum vector ***k***. It provides a potential barrier which is just large enough to avoid penetration. The MQQT DCSs were found to reproduce the QM DCSs obtained on the full PES more exactly than those obtained from the existing RQQT. In RQQT $V(R,\gamma_R)$ is approximated by a single hard shell contour $V(R,\gamma_R) = E_{col}$ so that the same hard shell PES is encountered for both a glancing impact and a head on impact. Interesting, except for lower Δj inelastic transitions the MQQT was found to produce quite similar DCSs to those obtained via the RQQT. Even at these lower values of Δj, the overall structure of the MQQT DCSs resembles the exact QM results obtained for the He + NO(X, j=½) collision system. The similarity of the scattering angle dependence of RQQT, MQQT and exact QM state resolved rotationally inelastic DCSs at higher Δj (and for lower Δj, excluding forwards directed scattering angles) has been shown to relate to the specific properties of the state of the art *ab initio* He + NO(X, v=0) PES[10], which assumes the bond length of NO molecule remains fixed at its equilibrium length $r = r_e$. The anisotropic Legendre coefficients $C_n(\cos\beta)$ become essentially stationary for potential energy

contours $V(R,\gamma_R) > 326cm^{-1}$, while the isotropic coefficient $C_{n=0}(\cos\beta)$, related to the effective size of the ellipsoid, increases steeply with $\cos^2\beta$.

Recently Cappelletti and co-workers provided experimental and quantum chemical evidence that charge transfer (CT) occurs between the molecular collision partners H_2O-Ne, Ar, Kr, Xe, H_2 and NH_3-H_2 at distances in the well region of the PES, causing the molecules to adiabatically adapt their bond geometry in a way that enhances the attractive intermolecular interaction.[26-31] This model was based on potential parameters obtained from the experimentally observed collision energy dependence of the glory amplitude of the integral collision cross section, and from CT calculations based on a general theoretical model which reproduces very accurately the collision cross sections obtained at the CCSD(T) level using large basis sets.[29] The CT contribution to the intermolecular PES was found to depend strongly on the molecular orientation (*i.e.* γ_R)[31] and increases with the proximity of collision partners.[29] The calculated CT contribution for the H_2O-RG complex were found to be almost negligible for He-H_2O but increased strongly with the mass of the RG atom.[32] These CT contributions to the intermolecular PES were taken into account in the *ab initio* PESs employed to predict the quantum state selected experimentally observed H_2-H_2O,-HDO and-D_2O rotationally inelastic DCSs.[33-35]

Whether the unpaired electron in the π* orbital of the NO(X) molecule is able to participate in electron transfer to a RG atom at distances smaller than the well region has not yet been explored. The theoretically predicted values of the rate constants of depolarization of selected NO($X^2\Pi_{½}$,v=0,j) levels in a thermal bath of Ar atoms computed on the highest quality UCCD(T) PESs,[9] (as obtained by Alexander with NO bond length fixed at its equilibrium value), were found to be significantly less than those obtained from experimental observation.[23] This discrepancy between experiment and theory is still to be explained.

Examples of experimental quantum state resolved rotationally inelastic DCSs for which MQQT could offer additional insight are:

1) Hexapole quantum state selected NO scattered from He at E_{col}= 510cm^{-1} (63.2 meV).[13]

2) Hexapole quantum state selected OH scattered from Ar at E_{col}= 500cm^{-1} (62.0meV), and from He at E_{col} = 460cm^{-1} (57.0 meV).[36]

3) Electronically resonant quantum state specific excited NO(v = 0, N = 0, $A^2\Sigma^+$) scattered from Ar,[37] He[38, 39] and Ne[39, 40] at respectively E_{col} = 855 cm^{-1} (230meV), E_{col} = 382 cm^{-1}(47.4 meV) and E_{col} = 488 cm^{-1}(60.5meV).

4) Asymmetric top H_2O supersonically cooled down to its *para* and *ortho* rotational ground states scattered from He at E_{col} = 429 cm^{-1} (53.5 meV)[33, 41].

5) H_2O and its isotopomers scattered from He, and from *para* j=0 and *ortho* j=1 H_2 at collision energies around 500 cm^{-1} (62 meV).[33-35]

6) Hexapole quantum state selected NO(X) scattered from Ar at E_{col} =530 cm^{-1} (66 meV)[5, 42] and from Ne at E_{col} = 540 cm^{-1} (68meV).[16] These latter experimental results offered an additional level of detail by including the scattering angle dependent alignment of the rotational angular momentum of the NO molecule following a rotationally inelastic collision,[43] and were all found to agree well with quantum mechanically exact and QQT predictions.[9, 44, 45]

7) Most recently, hexapole quantum state selected ND_3 scattered from He at E_{col}= 430cm^{-1} (51.8 meV)[46] and quantum state selective rotationally inelastic DCSs of the reactive CH_3 and CD_3 radicals scattered from He at 425 cm^{-1} (52.7 meV) and 440 cm^{-1} (54.6 meV) respectively.[25]

It is expected that in the near future, as pioneered by Tkáč et al,[46] such studies will become possible over an extended range of experimental collision systems which may be even more chemically distinct than those explored thus far.[4-6, 8, 11-14, 16, 21, 22, 33-38, 40-42, 47-50] The modified QQT model proposed in this work is presented as a potentially valuable tool by which further insight can be obtained into the nature of the collision energy dependent quantum mechanical interference phenomena that play an important role in molecular rotationally inelastic scattering events. The QQT treatment is quite versatile, being applicable to any collision between a particle and a linear or (a)symmetric top rotor, provided that the collision energy employed is significantly greater than the attractive interactions existing between the two particles. Because it directly calculates the differential cross-section from the scattering amplitude, without recourse to the intermediate of the scattering matrix produced by most quantum mechanical methods, it also offers an alternative physical insight into the scattering

problem, which may be of use in the interpretation and understanding of the collision dynamics.

In summary, the Modified QQT provides additional insight into the relation between the V_{sum} NO(X)-He PES and the rotationally inelastic quantum state resolved QM exact DCSs, by quantifying the effective shape of the equivalent hard shell PES experienced by the atom-diatom system during the course of the collision. The differences between the rotationally inelastic RQQT and MQQT DCSs and ICSs are expected to be more dramatic when the anisotropy of the repulsive PES contour exhibits a more significant dependence on the effective collision energy. There is a substantial variety of linear and non linear molecules for which quantum state resolved DCSs for collisions with Rare gas atoms or quantum state selected target molecules have been (or are being) explored. Modified QQT will prove a useful and numerically inexpensive tool to acquire insight into the repulsive regions of the PES that are most instrumental in determining the scattering dynamics, and most responsible for any differences observed between the theoretically predicted and experimentally observed DCSs.

Supplementary Information A detailed epressions for the MQQT method regarding the phase shift, legendre expansion coefficents, DCSs and ICSs is provide in the supporting information, along with a more detailed discussion of the Legendre moments and the scattering amplitude of a partially concave shell.

Acknowledgements This work is supported by the National Natural Science Foundation of China under Grant No. 11034003 and NO.91221301.

References:

1. A. Gijsbertsen, H. Linnartz, C. A. Taatjes and S. Stolte, *Journal of the American Chemical Society*, 2006, **128**, 8777-8789.
2. J. J. van Leuken, J. Bulthuis, S. Stolte and J. G. Snijders, *Chemical Physics Letters*, 1996, **260**, 595-603.
3. M. J. L. de Lange, M. Drabbels, P. T. Griffiths, J. Bulthuis, S. Stolte and J. G. Snijders, *Chemical Physics Letters*, 1999, **313**, 491-498.

4. M. J. L. de Lange, S. Stolte, C. A. Taatjes, J. Kłos, G. C. Groenenboom and A. van der Avoird, *The Journal of Chemical Physics*, 2004, **121**, 11691-11701.
5. C. J. Eyles, M. Brouard, C. H. Yang, J. Kłos, F. J. Aoiz, GijsbertsenA, A. E. Wiskerke and S. Stolte, *Nature Chemistry*, 2011, **3**, 597-602.
6. C. J. Eyles, M. Brouard, H. Chadwick, F. J. Aoiz, J. Kłos, A. Gijsbertsen, X. Zhang and S. Stolte, *Physical Chemistry Chemical Physics*, 2012, **14**, 5420-5439.
7. A. Ballast, A. Gijsbertsen, H. Linnartz and S. Stolte, *Molecular Physics*, 2008, **106**, 315-331.
8. A. Gijsbertsen, H. Linnartz and S. Stolte, *The Journal of Chemical Physics*, 2006, **125**, 133112-133110.
9. M. H. Alexander, *The Journal of Chemical Physics*, 1999, **111**, 7426-7434.
10. J. Kłos, G. Chalasinski, M. Berry, R. Bukowski and S. Cybulski, *J. Chem. Phys.*, 2000, **112**, 2195-2203.
11. C. A. Taatjes, A. Gijsbertsen, M. J. L. de Lange and S. Stolte, *J. Phys. Chem. A*, 2007, **111**, 7631-7639.
12. K. T. Lorenz, D. W. Chandler and G. C. McBane, *The Journal of Physical Chemistry A*, 2002, **106**, 1144-1151.
13. A. Gijsbertsen, H. Linnartz, G. Rus, A. E. Wiskerke, S. Stolte, D. W. Chandler and J. Kłos, *The Journal of Chemical Physics*, 2005, **123**, 224305-224314.
14. X. Zhang, C. J. Eyles, C. A. Taatjes, D. Ding and S. Stolte, *Physical Chemistry Chemical Physics*, 2013, **15**, 5620-5635.
15. *The typical calculation times of the MQQT and RQQT computer programs are under 30 seconds, performed on an 8Gb dual-core processor*.
16. M. Brouard, H. Chadwick, C. J. Eyles, B. Hornung, B. Nichols, J. M. Scott, F. J. Aoiz, J. Kłos, S. Stolte and X. Zhang, *Molecular Physics*, 2013, **111**, 1759-1771.
17. J. Kłos, F. J. Aoiz, J. E. Verdasco, M. Brouard, S. Marinakis and S. Stolte, *The Journal of Chemical Physics*, 2007, **127**, 031102-031104.
18. F. J. Aoiz, J. E. Verdasco, M. Brouard, J. Kłos, S. Marinakis and S. Stolte, *J. Phys. Chem. A*, 2009, **113**, 14636-14649.
19. D. Chandler and P. Houston, *J. Chem. Phys.*, 1987, **87**, 1445-1447.
20. A. Eppink and D. Parker, *Rev. Sci. Instrum.*, 1997, **68**, 3477-3484.
21. K. Thomas Lorenz, M. S. Westley and D. W. Chandler, *Physical Chemistry Chemical Physics*, 2000, **2**, 481-494.
22. E. A. Wade, K. T. Lorenz, J. L. Springfield and D. W. Chandler, *The Journal of Physical Chemistry A*, 2003, **107**, 4976-4981.
23. G. Paterson, A. Relf, M. L. Costen, K. G. McKendrick, M. H. Alexander and P. J. Dagdigian, *The Journal of Chemical Physics*, 2011, **135**, 2343064 p2343061-2343011.
24. V. Khare, D. J. Kouri and D. K. Hoffman, *The Journal of Chemical Physics*, 1982, **76**, 4493-4501.
25. O. Tkac, A. G. Sage, S. J. Greaves, A. J. Orr-Ewing, P. J. Dagdigian, Q. Ma and M. H. Alexander, *Chemical Science*, 2013, **4**, 4199-4211.
26. V. Aquilanti, E. Cornicchi, M. Moix Teixidor, N. Saendig, F. Pirani and D. Cappelletti, *Angewandte Chemie International Edition*, 2005, **44**, 2356-2360.
27. L. Roncaratti, L. Belpassi, D. Cappelletti, F. Pirani and F. Tarantelli, *The Journal of Physical Chemistry A*, 2009, **113**, 15223-15232.
28. L. Belpassi, F. Tarantelli, F. Pirani, P. Candori and D. Cappelletti, *Physical Chemistry Chemical Physics*, 2009, **11**, 9970-9975.
29. L. Belpassi, M. L. Reca, F. Tarantelli, L. F. Roncaratti, F. Pirani, D. Cappelletti, A. Faure and Y. Scribano, *Journal of the American Chemical Society*, 2010, **132**, 13046-13058.

30. D. Cappelletti, E. Ronca, L. Belpassi, F. Tarantelli and F. Pirani, *Accounts of Chemical Research*, 2012, **45**, 1571-1580.
31. F. Pirani, D. Cappelletti, L. Belpassi and F. Tarantelli, *The Journal of Physical Chemistry A*, 2013, **117**, 12601-12607.
32. C. Amiot, *Journal of Molecular Spectroscopy*, 1982, **94**, 150-172.
33. C. Yang, G. Sarma, J. J. ter Meulen, D. H. Parker, G. C. McBane, L. Wiesenfeld, A. Faure, Y. Scribano and N. Feautrier, *J. Chem. Phys.*, 2010, **133**, 131103.
34. C. H. Yang, G. Sarma, D. H. Parker, J. J. ter Meulen and L. Wiesenfeld, *The Journal of Chemical Physics*, 2011, **134**, 204308-204312.
35. G. Sarma, C.-H. Yang, A. K. Saha, D. H. Parker and L. Wiesenfeld, *The Journal of Chemical Physics*, 2013, **138**, 024314-024319.
36. G. Sarma, S. Marinakis, J. J. ter Meulen, D. H. Parker and K. G. McKendrick, *Nat Chem*, 2012, **4**, 985-989.
37. J. J. Kay, G. Paterson, M. L. Costen, K. E. Strecker, K. G. McKendrick and D. W. Chandler, *J. Chem. Phys.*, 2011, **134**, 091101.
38. J. J. Kay, J. D. Steill, J. Kłos, G. Paterson, M. L. Costen, K. E. Strecker, K. G. McKendrick, M. H. Alexander and D. W. Chandler, *Molecular Physics*, 2012, **110**, 1693-1703.
39. J. Kłos, M. H. Alexander, R. Hernandez-Lamoneda and T. G. Wright, *The Journal of Chemical Physics*, 2008, **129**, 244303-244312.
40. J. D. Steill, J. J. Kay, G. Paterson, T. R. Sharples, J. Kłos, M. L. Costen, K. E. Strecker, K. G. McKendrick, M. H. Alexander and D. W. Chandler, *The Journal of Physical Chemistry A*, 2013, **117**, 8163-8174.
41. C.-H. Yang, G. Sarma, J. J. ter Meulen, D. H. Parker, U. Buck and L. Wiesenfeld, *The Journal of Physical Chemistry A*, 2010, **114**, 9886-9892.
42. C. J. Eyles, M. Brouard, H. Chadwick, B. Hornung, B. Nichols, C. H. Yang, J. Kłos, F. J. Aoiz, A. Gijsbertsen, A. E. Wiskerke and S. Stolte, *Physical Chemistry Chemical Physics*, 2012, **14**, 5403-5419.
43. M. Brouard, H. Chadwick, C. J. Eyles, B. Hornung, B. Nichols, F. J. Aoiz, P. G. Jambrina and S. Stolte, *The Journal of Chemical Physics*, 2013, **138**, 104310-104313.
44. M. Brouard, H. Chadwick, C. J. Eyles, B. Hornung, B. Nichols, F. J. Aoiz, P. G. Jambrina, S. Stolte and M. P. de Miranda, *The Journal of Chemical Physics*, 2013, **138**, 104309-104315.
45. M. H. Alexander, P. Soldan, T. G. Wright, Y. Kim, H. Meyer, P. J. Dagdigian and E. P. F. Lee, *The Journal of Chemical Physics*, 2001, **114**, 5588-5597.
46. O. Tkáč, A. K. Saha, J. Onvlee, C.-H. Yang, G. Sarma, C. K. Bishwakarma, S. Y. T. v. d. Meerakker, A. v. d. Avoird, D. H. Parker and A. J. Orr-Ewing, *Phys. Chem. Chem. Phys.*, 2014, **16**, 477-488.
47. J. J. Kay, S. Y. T. van de Meerakker, E. A. Wade, K. E. Strecker and D. W. Chandler, *The Journal of Physical Chemistry A*, 2009, **113**, 14800-14806.
48. J. J. Gilijamse, S. Hoekstra, S. Y. T. van de Meerakker, G. C. Groenenboom and G. Meijer, *Science*, 2006, **313**, 1617-1620.
49. L. Scharfenberg, J. Kłos, P. J. Dagdigian, M. H. Alexander, G. Meijer and S. Y. T. van de Meerakker, *Physical Chemistry Chemical Physics*, 2010, **12**, 10660-10670.
50. L. Scharfenberg, K. B. Gubbels, M. Kirste, G. C. Groenenboom, A. Avoird, G. Meijer and S. Y. T. Meerakker, *Eur. Phys. J. D*, 2011, **65**, 189-198.
51. M. Brouard, B. Hornung and F. J. Aoiz, Physical Review Letters, 2013, **111,** 183202 p.1-5.

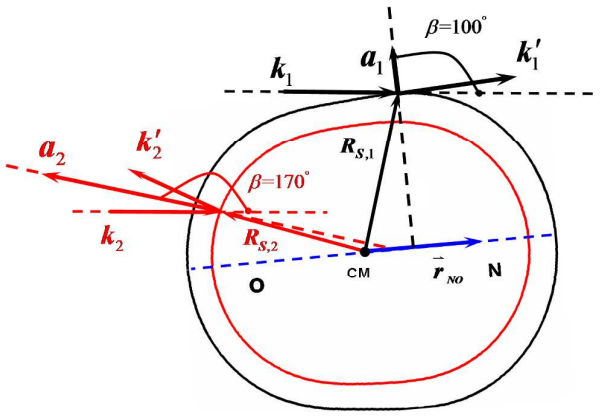

Figure 1. Illustration of the relationship between the modified QQT hard shell contour and the polar angle β between the solid apse vector $\boldsymbol{a}$ (extended by a dashed line) and the incoming wave vector $\boldsymbol{k}$. The blue NO axis vector $\vec{r}$ is extended by a dashed blue line. The $\beta = 100°$ contour corresponds to nearly perfect forward scattering and $\beta = 170°$ to nearly perfect backwards scattering. The red and black shell circumferences correspond respectively to $R_S^{\mathrm{mod}}[\cos\gamma_R; \cos(\beta = 170°)]$ and to $R_S^{\mathrm{mod}}[\cos\gamma_R; \cos(\beta = 100°)]$. Note that the forward scattering $\beta = 100°$ shell exhibits a slightly concave shape at its waist.

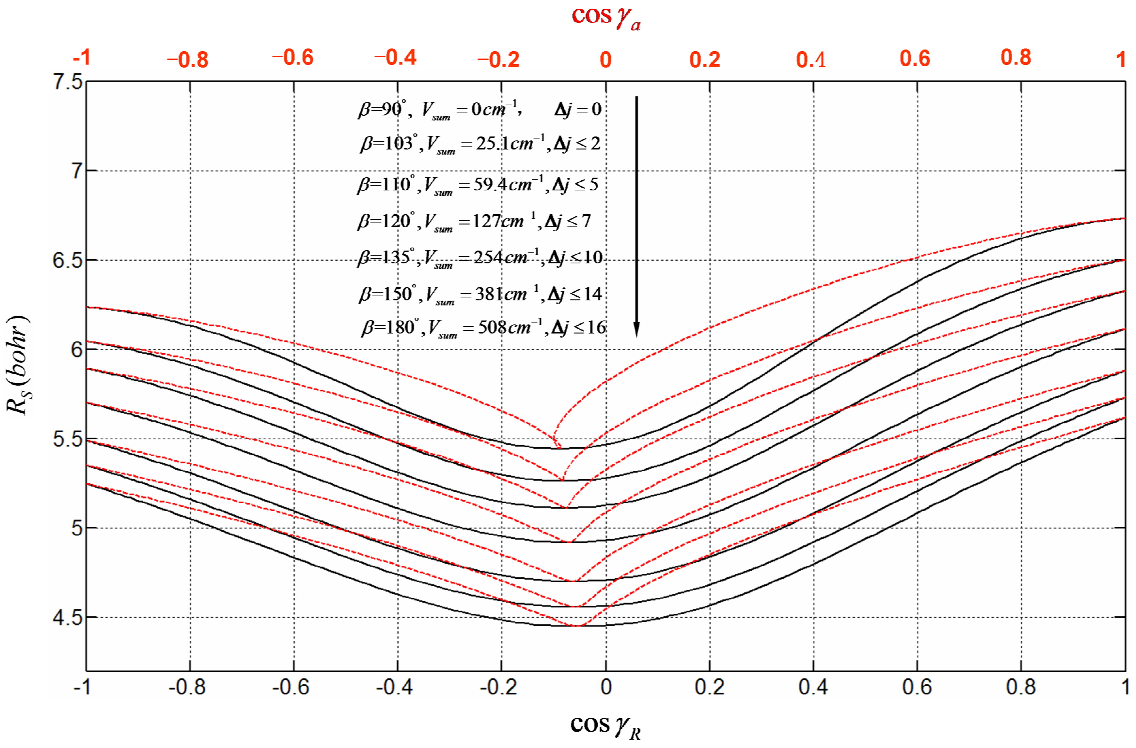

Figure 2. The hard shell contours $R_S^{\mathrm{mod}}(\cos\gamma_R;\cos\beta)$ of the He-NO(X) modified hard shell as a function of $\cos\gamma_R$ (solid black lines) at E_{col} = 508 cm^{-1} for a number of specified kinematic apse angles β. These same contours are also displayed as a function of $\cos\gamma_a$ (dotted red lines). The waist of the potential contours $R_s(\cos\gamma_R,\cos\beta)$ does not occur at $\cos\gamma_a = 0$ but at a slightly negative offset for $\cos\gamma_a$, shifted towards the O-end of the NO(X) molecule. This offset decreases as the apse angle β increases. Note that between $\cos\beta = \cos\beta_{\min}^{convex} = -0.19842$ and $\cos\beta = 0$ it is impossible to assign a unique value of R_S to the values of $\cos\gamma_a$ near the waist of the potential contours. In the range $90° \le \beta < \beta_{\min}^{convex} = 101.45°$ the $R_S^{\mathrm{mod}}(\cos\gamma_a;\cos\beta)$ functionality at about $\cos\gamma_a \approx -0.05$ is no longer single valued. The MQQT range of allowed Δj values for a particular hard shell contour as well the associated values of β are indicated.

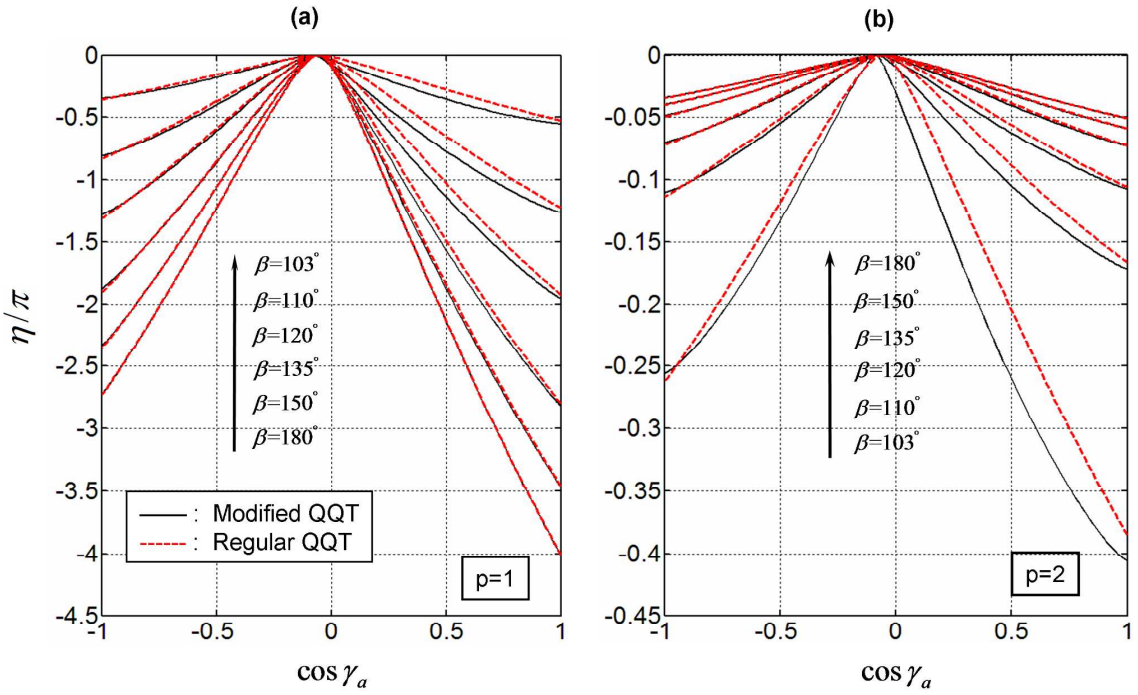

Figure 3. The modified $\eta^{\mathrm{mod}}_{j=0.5\to j'=2.5}(\gamma_a;\beta)/\pi$ and regular $\eta^{reg}_{j=0.5\to j'=2.5}(\gamma_a;\beta)/\pi$ QQT phase shift curves for the rotationally inelastic $j=\frac{1}{2}\to j'=\frac{7}{2}$ transition of He + NO(X) at E_{col} = 508 cm^{-1} for $\beta=103°$, 110°, 120°, 135°, 150° and 180°, which respectively correspond to $\theta=15.0^{\circ}$, 35.5°, 57.3°, 88.5°, 119.1° and 180° in the classically allowed (p=1) left panel and to $\theta=11.1^{\circ}$, 4.55°, 2.66°, 1.55°, 0.85° and 0° in the classically forbidden(p=2) right panel. Note that $\beta\geq\beta_\kappa=102.84°$ or $\cos\beta\leq\cos\beta_\kappa=0.22204$. The p=2 QQT phase shifts relate to the p=1 values via a β and $E_{j'}/E_{col}$ dependent proportionality factor which ranges from unity at $\cos\beta=\cos\beta_\kappa$ to 0.01266 at $\cos\beta=-1$ as follows directly from Eq.(I.5) of the ESI.

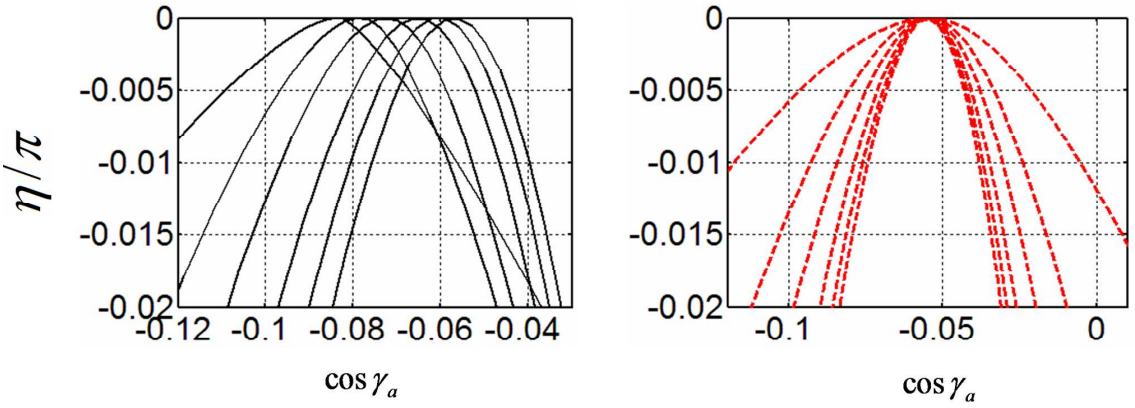

Figure 4. Details of the classically allowed (p=1) NO-He phase shift curves η/π around $\cos\gamma_a = \cos\gamma_a^{waist}$ of the Modified (left panel) and Regular (right panel) QQT which remain unresolved in Figure 3. Note that the value of $\cos\gamma_a^{waist}$ at the maximum $\eta/\pi = 0$ was found to be equal to -0.082 at β = 103º, -0.076 at β = 110º -0.071 at β = 120º, -0.065 at β = 135º, -0.058 at β = 150º and -0.055 at $\beta = \beta_{max}$ = 180º. The maximum shifts towards that of the homonuclear limit of $\cos\gamma_a^{waist} = 0$ as β increases from 100° to 180°. Such a shift remains absent in the right panel, since RQQT assumes a hard shell PES which is equal to that of MQQT at $\beta = \beta_{max}$ = 180º for all β.

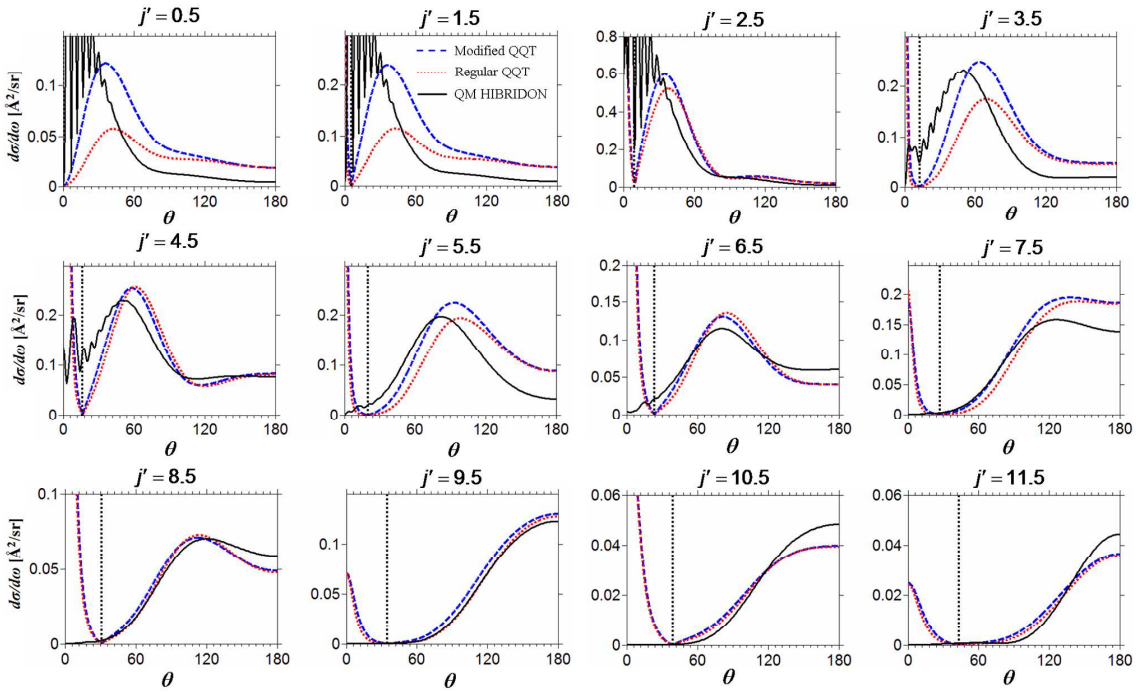

Figure 5. The QM HIBRIDON (black solid lines), MQQT (blue dashed lines) and RQQT (red dotted lines) DCSs for the NO(X)+He transitions $j=\frac{1}{2},\varepsilon=-1\rightarrow j'=\frac{1}{2},\varepsilon'=1$ and $j=\frac{1}{2},\varepsilon=-1\rightarrow 1.5\le j'\le 11.5,\varepsilon'=-1$ at a collision energy of 508cm^{-1}. The exact QM DCSs are scaled to the regular QQT model DCSs as described in the main text. The black dotted vertical line separates the classical forbidden (p=2), $\theta<\theta_\kappa$ range of scattering angles from those that are classical allowed (p=1) with $\theta\ge\theta_\kappa$.

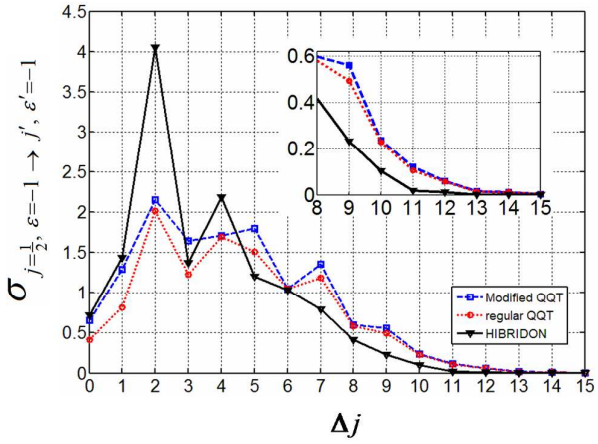

Figure 6. Comparison between the QM (▼), modified QQT (■) and regular QQT (●) quantum state resolved rotationally inelastic integral cross sections for NO-He at a collision energy of 508cm^{-1}. Note that as in Fig. 5 the Δj=0 differential cross section corresponds to an $\varepsilon = -1 \to \varepsilon' = 1$ transition while for all others $\varepsilon = -1 \to \varepsilon' = -1$. The similarity of the MQQT and RQQT ICSs at $\Delta j \geq 10$ complies with the similarity of the DCSs depicted in Fig.5.